Title

Combining automated mineralogy with X-ray computed tomography: Internal characterization of ore samples at the microscopic scale.

Author information

Florian Buyse[a, d], Stijn Dewaele[b], Matthieu N. Boone[c, d], Veerle Cnudde[a, d, e]

[a]Pore-Scale Processes in Geomaterials Research group (PProGRess), Department of Geology, Ghent University, Krijgslaan 281/S8, B-9000 Ghent, Belgium

[b]Laboratory for Mineralogy and Petrology, Department of Geology, Ghent University, Krijgslaan 281/S8, B-9000 Ghent, Belgium

[c]Radiation Physics Research Group, Department of Physics and Astronomy, Ghent University, Proeftuinstraat 86/N12, B-9000 Ghent, Belgium

[d]Centre for X-ray Tomography (UGCT), Ghent University, Proeftuinstraat 86, B-9000 Ghent, Belgium

[e]Environmental Hydrogeology, Department of Earth Sciences, Utrecht University, Princetonlaan 8a, 3584 CB Utrecht, The Netherlands

Corresponding author: florian.buyse@ugent.be (ORCID: 0000-0002-3515-868X)

ORCID of the authors

F. Buyse: 0000-0002-3515-868X S. Dewaele: 0000-0002-8805-6986

M. N. Boone: 0000-0002-5478-4141 V. Cnudde: 0000-0002-3269-5914

Abstract

Advanced chemical and mineralogical techniques are necessary to further our understanding of ore deposits and their genesis. Using X-ray micro-computed tomography (µCT) and an automated mineralogy (AM) system based on scanning electron microscopy with an energy dispersive X-ray spectrometer (SEM-EDX), we investigated the internal mineralogy of Sn-Nb-Ta pegmatites. This paper presents a comprehensive methodology to quantify and visualize the mineral relationships of ore samples in three-dimensional space at the microscopic scale. A list of all possible minerals present, a

so-called mineral library, was deduced with a SEM-based AM system and served as the ground truth for the interpretation of µCT data. A reconstructed attenuation coefficient (μ_{rec}) was calculated for mineral phases that have been identified and provided a most correct guidance to differentiate between minerals for a given experimental µCT setup. Despite some limitation in sample size and mineral identification, these complementary techniques enabled the differentiation of a Fe-Li mica from biotite based on the chemical attribution of lithium to μ_{rec}. Using statistical descriptors, we quantified the general orientation of individual mineral phases and their spatial correlation to comply with the needs of processing large datasets at a low computational expense. Applying this comprehensive methodology to a case study demonstrates the possibilities of combining a SEM-based AM system with µCT analysis to investigate ore samples at the microscopic scale.

Keywords

X-ray computed tomography, automated mineralogy, mineral texture, correlative microscopy, pegmatites

INTRODUCTION

In this ever-changing world, we are more and more confronted with the challenges of future mineral supply to an accelerating global population growth (Ali et al., 2017). In addition, modern society relies increasingly on the development of renewable energy sources and other high technology applications that require not only a vast amount of common commodities (e.g., copper, steel), but also a growing number of critical low-volume elements (Hayes & McCullough, 2018; Wellmer et al., 2019). The detailed characterization of the morphology, texture, mineralogy, and chemistry of different desirable minerals, but also the bulk minerals in which they are embedded, plays an important role in the optimal recovery of critical raw materials (Reuter et al., 2019).

The mineralogical study of ore deposits conventionally relies on the macroscopic observations of hand specimens collected during fieldwork and on microanalytical two-dimensional (2D) techniques to characterize the chemical, mineralogical, and structural variations of millimeter- to centimeter-sized samples, and this with a spatial resolution down to the microscopic scale (Pearce et al., 2018). Microscopic observations are often limited to optical microscopy and different microbeam analytical techniques, combined with integrated imaging techniques like scanning electron microscopy (SEM).

SEM is often assisted by 2D elemental mapping using energy-dispersive (EDX) or wavelength-dispersive (WDX) X-ray spectrometers or complemented with data from an electron probe microanalyzer (EPMA) acting as an analytical tool to non-destructively determine the chemical composition of small volumes of solid materials (Reed, 2005). SEM may also be combined with a focused ion beam (FIB-SEM) for serial FIB milling of the sample surface to acquire a sequence of cross-sectional SEM images and thus a three-dimensional (3D) visualization of the sample (Gu et al., 2020). Often, additional structural and analytical chemical methods, such as X-ray diffraction (XRD) and X-ray fluorescence (XRF), are used to determine the mineralogical and chemical composition of the samples.

Although these techniques are well-known and commonly used for the characterization of geological samples, there is a need for non-destructive characterization that provides in 3D the structural, mineralogical, and chemical composition of the interior of geological samples (Wang & Miller, 2020). The accurate 3D mineralogical and geochemical characterization is crucial for improving the understanding of ore genesis (Godel, 2013), and is particularly applicable to petrological and genetic investigations of low-grade fine-grained ore deposits or nugget-type of mineralization (Kyle & Ketcham, 2015). This urges the need for the development of new and innovative technologies for adequate ore characterization (Becker et al., 2016; Gessner et al., 2018) and associated data analysis (Guntoro et al., 2019a).

X-ray micro-computed tomography (µCT) is a non-destructive X-ray imaging technique that allows for the analysis of the interior of geological samples in 3D. This technique has the ability to eliminate the stereological errors from conventional 2D image analysis and to leave the samples intact for further sample characterization (Guntoro et al., 2019a). This offers the possibility to study mineral relationships in 3D (e.g., Jardine et al., 2018) and acquire quantitative estimations of mineral shape, size, and orientation (e.g., Ketcham & Mote, 2019). The principle of µCT is based on the calculation of the X-ray linear attenuation coefficient (μ_{lin}), which depends on the material properties (effective atomic number, density) and the incident energy of the X-ray beam. Typical geological sample sizes for µCT imaging are between 1 mm and 5 cm (Cnudde & Boone, 2013), where a trade-off has to be made between the transmitted X-ray photon flux and resolution. The application potential of this technique has been reviewed within geosciences (Cnudde & Boone, 2013; Kyle & Ketcham, 2015; Wang & Miller, 2020) and has established its place in the contribution to geological studies. Processed µCT data provides images of the mineral relationships in 3D together with statistical parameters that are of interest for studies of

ore-forming processes, extractive metallurgy, and metal production engineering (Pearce et al., 2018; Wang & Miller, 2020). Since the main drawback of standard µCT is the absence of chemical information, it is currently only possible to segment various compounds based on different X-ray attenuation and/or shape properties (Gunturo et al., 2019a).

Despite continuous technological and computational advances (Wang & Miller, 2020), most applications in mineral characterization are rather limited to the 3D segmentation between the major phases, i.e., pores, low-density phases, and high-density phases (Guntoro et al., 2019a). Therefore, recent work in µCT focuses on the development of image post-processing procedures (Becker et al., 2016; Guntoro et al., 2019b), whether or not together with complementary microscopic techniques (De Boever et al., 2015; Laforce et al., 2016; Reyes et al., 2017; Warlo et al., 2021), to differentiate between complex intergrown mineral phases. In the future, the integration of machine learning and artificial intelligence is considered to be crucial for the generation of mineralogical information from standard µCT data (Guntoro et al., 2019a). Various techniques have been developed to extract mineral features from µCT datasets (Jardine et al., 2018). Existing techniques are, however, currently limited to the computational expense of processing large datasets (Guntoro et al., 2019a) and are just now slowly starting to emerge (e.g., Strzelecki et al., 2021).

This study aims to develop a comprehensive methodology by combining state-of-the-art µCT and an SEM-based automated mineralogy (AM) system to characterize the mineralogy of ore samples in 3D. We present a test study on pegmatite-hosted Sn-Nb-Ta mineralization from the Mesoproterozoic orogenic belts of Central Africa (Dewaele et al., 2011; Melcher et al., 2015), where we will overcome some of the traditional issues to characterize the internal geochemical and mineralogical composition in 3D at the microscopic scale.

MATERIALS AND METHODS

Samples

Samples were selected from the intensively studied Sn-Nb-Ta mineralization of the Gatumba area in western Rwanda, Central Africa (Lehmann et al., 2008; Dewaele et al., 2011; Hulsbosch et al., 2013; Lehmann et al., 2014; Hulsbosch & Muchez, 2020). This mineralization consists of millimeter-sized cassiterite and columbite-tantalite minerals hosted within much less dense gangue minerals (mainly quartz, feldspars, and muscovite) (Dewaele et al. 2011). In an individual pegmatite, a mineralogical and

geochemical zonal development is observed from margin towards the center, with a hydrothermal overprint completely altering the original pegmatite composition at some locations, (Dewaele et al., 2011; Hulsbosch & Muchez, 2020). The exact spatial relationship between the different ore minerals is difficult to observe with standard techniques, and not exactly known.

In addition to representative polished sections with a higher concentration of ore minerals for reflected light microscopy and SEM-based AM analyses, rock samples were specifically prepared for µCT analysis. Since cylindrical samples have the most efficient geometry for the cone beam configuration employed in most modern laboratory µCT systems (Kyle & Ketcham, 2015), drilled core samples were made (2 cm in diameter). These drilled core samples were afterwards also prepared to be suitable for further analyses with optical microscopy and SEM-based AM (i.e., polishing of the top and bottom surface). Results will be further discussed by means of two representative cylindrical samples A and B acquired from one of the pegmatite samples from the Gatumba area, of which sample A is used as an example to discuss the process of 3D mineral phase segmentation and feature extraction.

Optical and Scanning Electron Microscopy

Reflected light microscopy was carried out at Ghent University, using a Nikon Eclipse LV100N POL polarizing petrographic microscope, as a preliminary step to identify Sn-Nb-Ta-(W)-bearing ore minerals and their interrelationships (e.g., identification of possible mineral inclusions). SEM-EDX was performed at Ghent University using TESCAN Integrated Mineral Analyzer (TIMA-X) equipped with a field emission gun and one EDX detector. TIMA-X is a system optimized to rapidly acquire low-count spectra (Hrstka et al., 2018) and combines calibrated back-scattered electron (BSE) imaging and EDX analysis for mineral classification training using an AM system. The mineral distribution maps are based on the comparison of EDX spectra obtained from each pixel with a classification scheme, where a set of rules are designated to the calibrated line intensities of the different elements (see also Hrstka et al., 2018). The working conditions were: an acceleration voltage of 25 kV, a working distance of 15.0 mm, and a spatial resolution between 9 and 18 µm for both BSE images and EDX spectra. The energy resolution of the EDX spectra, as measured at Mn Kα, was ±140 eV. The acquired mineralogical information serves as a mineral library for the interpretation of the µCT data.

X-ray Micro-Computed Tomography (µCT)

The µCT analyses were performed at the Ghent University Centre for X-ray Tomography (www.ugct.ugent.be). The High-Energy CT system Optimized for Research or HECTOR (Masschaele et al., 2013) was used under the scanning conditions as summarized in Table 1. Reconstructions of the projectional radiographs, acquired using the traditional cone-beam µCT setup, were performed with the Octopus reconstruction software (Vlassenbroeck et al., 2007). This software tool allows for pre-processing corrections (e.g., flat field correction and ring filter) and corrections during the reconstruction (e.g., beam hardening correction). Image analysis was executed in the Fiji/ImageJ software (Schindelin et al., 2012) using a 3D trainable Weka Segmentation plugin (Arganda-Carreras et al., 2017) for the mineral phase segmentation and by using executable scripts to automate certain repetitive steps. The different steps that were undertaken to investigate the different mineral phases in 3D are discussed below and summarized in Fig. 1.

Information about the mineralogical composition was obtained during optical microscopy and TIMA-X analyses of the polished sections and was supplemented by observations from previous research (Lehmann et al., 2008; Dewaele et al., 2011; Hulsbosch et al., 2013; Melcher et al., 2015; Hulsbosch & Muchez, 2020). The mineralogical composition, material density (ρ), and X-ray energy determine the linear attenuation coefficient (μ_{lin}) and provide insight into the capability of µCT to segment minerals with a similar attenuation (Fig. 2a). However, in lab-based µCT a polychromatic source is used and the energy dependency of μ_{lin} needs to be taken into account. Therefore, the theoretical μ_{lin} was recalculated for the given experimental setup (Table 1) using the in-house developed software Arion (Dhaene et al., 2015). This value is hereafter referred to as the reconstructed attenuation coefficient (μ_{rec}). The calculations of μ_{rec} take into account the spectral sensitivity of the detector and the effects (e.g., metal artifacts and beam hardening) induced by the polychromaticity of the X-ray source. Therefore, properties like sample size, shape, elemental composition and density are taken into account in the simulation tool. For a given setup, μ_{rec} serves as a more accurate depiction of the possible segmentation between the different mineral phases (e.g., μ_{rec} of schorl and apatite was here too similar to be segmented using this setup; Fig. 2b) and the interpretation of the different mineral interrelationships.

Despite the measures taken to prevent imaging artifacts (e.g., Al filter, beam hardening corrections during the reconstruction), and thus to eliminate μ_{rec} variability, the final µCT image vertically still displays variable grayscale values throughout the slices for the same mineral phase (see also Fig. 3 in Guntoro

et al., 2019b). A region of interest, including more than 80% of the dataset, was selected to avoid mineral phase segmentation issues.

Since the µCT images contain numerous mineral phases and, thus, numerous grey values (Fig. 3a), prior noise filtering was not considered, as the variance would also be taken into account during the segmentation step (see below). As a first step of data preparation, automatic thresholding of the data was performed with Otsu's method (Otsu, 1979) to separate the background from sample data. This was followed by a four times 1-pixel erosion operation (binary morphology) to avoid false segmentation at the sample borders that could not be resolved with beam hardening corrections (Fig. 3b). Segmentation was then performed using Weka 3D segmentation (Arganda-Carreras et al., 2017) within the Fiji environment where a set of 50 images was used to train the following features: edges (canny edge detection) and texture filters (mean, variance) in a fast random forest classifier. The training of the classifier was adopted iteratively by using input from corresponding mineral distribution maps acquired with TIMA-X until an accurate segmentation result was achieved on the subset (Fig. 3c). The trained classifier was then used to automatically segment each corresponding dataset (over 1000 images each). A tiling algorithm, reducing the memory requirements (Arganda-Carreras, 2018), was applied to prevent running into out-of-memory exceptions when processing large 3D datasets (> 3GB) on a regular desktop. Previously, this algorithm has already been successfully used in e.g., Callow et al. (2020). Post-processing steps were undertaken for each individual segmented phase to avoid partial volume effects at boundaries between two segmented phases (Fig. 3d). A boundary between a high-density phase and a low-density phase would be incorrectly interpreted as an intermediate density phase and was therefore removed from the data using binary morphology operations (see detailed excerpt in Fig. 3e-g).

Feature Extraction

Segmentation of the µCT images resulted in a dataset of labeled images, where each label represented the 3D volume of a segmented phase. The Pearson correlation coefficient (Eq. 1) was calculated to represent the interrelationships between two different segmented phases. This measure is defined as the ratio between the covariance of two variables and the product of their standard deviations. For two phases X and Y in (Eq. 1), metrics are calculated using the surface areas of two phases which are compared along a defined direction (see below) and are normalized after the total area of the sample

within each 2D slice (which translates as a comparison of area percentages). Values of the Pearson correlation coefficient may range between -1 (negative linear correlation) and 1 (positive linear correlation). A correlation coefficient of 0 implies that there is no linear dependency between the two phases in that direction.

$$\rho(X,Y) = \frac{cov(X,Y)}{\sigma(X)\sigma(Y)} \qquad \text{(Eq. 1)}$$

The coefficient of variation (Eq. 2) was calculated to represent the general orientation of each individual segmented phase. This measure is defined as the ratio of the standard deviation (σ) to the mean (μ) of the previously mentioned area percentages calculated along a defined direction. The unit of this measure is dimensionless and is thus of interest to compare numerical values of different populations with various averages. The interpretation of the data is based on the fact that higher values are obtained along the longitudinal axis of a phase and lower values are obtained perpendicular to this axis (see Fig. 4). Phases which have no preferential elongation/orientation, will display similar (low) values for each measured direction.

$$c_v = \frac{\sigma}{\mu} = \frac{\sqrt{\sum_i (x_i - \mu)^2 p(x_i)}}{\mu} \qquad \text{(Eq. 2)}$$

As previously mentioned, these statistical measures are calculated along a defined direction. Images are usually stored as a stack of virtual 2D slices perpendicular to the rotational axis or Z-axis, but calculations for the 2D slices along the Z-axis would only give 1D information. For a stereographic depiction of a possible variety in statistical measures along different predefined directions, and thus in 3D, the images needed to be resliced along all possible directions. Orientations will be presented in a spherical coordinate system using the azimuth on the XY plane and the inclination from the Z-axis (Fig. 5a). Using a spacing of 15° along the azimuth on the XY plane (360°) and the inclination from the Z-axis (90°) gives 175 predefined directions. A script was written in Fiji/ImageJ to automatically reslice the images over all predefined directions and calculate along each defined direction the surface areas for each segmented phase. Data is correspondingly represented in a polar rose chart using Plotly Python Open Source Graphing Library (Fig. 5b).

RESULTS

Mineral Distribution Maps

The mineral content of the drilled core samples (based on mineral distribution maps acquired with TIMA-X and sorted according to μ_{rec}; Fig. 2b) consists of kaolinite, beryl, albite, quartz, K-feldspar, muscovite,

Fe-Li mica, schorl, apatite, zircon, barite, and columbite-tantalite. The matrix occurring between the larger-sized minerals of these samples consisted almost entirely of quartz and albite, but often contained traces of K-feldspar occurring together with beryl. Muscovite is next to quartz and albite an important constituent and was observed to be often overgrown by an albite matrix (Fig. 6b). Muscovite may range in size from centimeter-size to aggregates of submillimeter-sized crystals. Kaolinite is closely associated with muscovite, but was only present in minor amounts. Besides muscovite (Fig. 7a), another mica was present to a much lesser extent and has been identified as an Fe-Li mica (Fig. 7b). Tourmaline occurs as grouped acicular crystals. EDX analyses of tourmaline showed significant amounts of Fe, Al, and to a lesser extent Na and Mg. Therefore, tourmaline was identified as a Fe-rich member of the schorl-dravite series (cf., Hulsbosch et al., 2013). Apatite mostly occurred as dispersed submillimeter-sized minerals within the matrix. One of the investigated polished sections of sample A rather displayed a grouped occurrence of apatite grains (Fig. 6b). Barite was observed as a small veinlet (400 µm) along the cleavage planes of muscovite and also as an inclusion within tourmaline. Small columbite-tantalite inclusions (18 µm) were observed in both the albite-quartz matrix and in association with muscovite grains. Cassiterite has not been observed during TIMA-X mapping.

X-ray Micro-Computed tomography (µCT)

Comparison of Mineral Distribution Maps with µCT Data

The µCT images of the drilled core samples (Fig. 6d) were interpreted by comparison with the equivalent mineral distribution maps acquired with TIMA-X (Fig. 6b) and by using the calculated μ_{rec} values of the occurring minerals for the given experimental setup (Fig. 6c).

The matrix of the samples consisted almost entirely of two phases that were close to each other in greyscale values, but were still visually distinguishable based on slight differences in greyscale values (Fig. 8a). These mineral phases were identified as quartz and albite and occurred as interconnected phases throughout the drilled core samples. The next main mineral phase identified in the µCT data was muscovite. Muscovite occurred as large centimeter-sized scaly mineral fragments, but also as much smaller fragments (often as stellate aggregates) disseminated in the matrix. It was often observed for the large scaly muscovite fragments that they were overgrown by a small border of albite matrix, regardless of being located within a quartz-rich matrix. Some of the larger muscovite fragments were altered and only displayed relicts of the original shape. K-feldspar was, similar to observations with

TIMA-X, found to be associated with beryl within the samples (Fig. 8a). Euhedral crystals of K-feldspar and beryl were only observed when occurring with(in) muscovite and/or neighbored by schorl. Apatite occurred mostly as a minor phase, but was widely distributed throughout the samples. Together with TIMA-X observations (see also Fig. 6), it was observed that apatite may occur as well as grouped fragments that were strongly intergrown with stellate aggregates of muscovite. Minor occurrences of dense minerals, which appeared to be mainly zircon grains, when compared with corresponding mineral distribution maps, were strongly correlated to these grouped occurrence of apatite grains. The prismatic/acicular crystal habit of schorl (Fig. 8a) allowed to differentiate these mineral fragments from apatite. Schorl was unaffected by the presence of other mineral phases and maintained its mineral shape. Clusters of schorl fragments are unobstructed by the presence of muscovite fragments nor of the main matrix constituents. One remarkable observation was the presence of a two centimeter long schorl fragment crosscutting sample B (Fig. 8a-b). There were several mineral phases associated with this schorl crystal, which were, from low density to high density, albite-muscovite-schorl or at least minerals with a similar grey value. Since this was an important observation, sample B was re-polished to acquire an additional mineral distribution map for this slice to confirm the µCT observations. It is important to note that next to albite, quartz was also identified as a low-density phase within this schorl crystal. The observed occurrence of a small barite vein as a possible mineral inclusion within a muscovite grain during TIMA-X analysis was confirmed to be a real mineral inclusion during µCT analyses.

Segmentation of Mineral Phases

Based on the observations acquired for the two samples and the predetermined μ_{rec} values (Fig. 2b), different phases were selected for segmentation using the proposed methodology. An example of a possible output for sample A is presented below.

The group of identified mineral phases was reduced to the following 5 segmented phases (from low to high μ_{rec}): albite, quartz, muscovite, schorl/apatite and dense mineral phases (Fig. 9), with a vol% of respectively 43.51, 43.43, 11.36, 1.60 and 0.04, with respect to the sample data after a first step of data preparation. The remaining 0.06 vol% was removed from the dataset through post-processing to remove false mineral phase identification at the boundaries between two segmented phases. The difference in greyscale value and μ_{rec} of schorl and apatite is limited. Apatite is expected to be only slightly higher in

greyscale value (see Fig. 2b) and were therefore grouped because of their similarity. The dense mineral phase consists of all identified mineral phases for which μ_{rec} is higher than the other segmented phases (i.e., denser than schorl/apatite). These phases included ore minerals and high-density accessory minerals (in particular zircon) that were observed during mineral mapping. It must be noted that this sample was also re-polished to chemically investigate the largest grain that was classified as a dense mineral phase using TIMA-X (Fig. 9). It, however, displayed relatively higher greyscale values, and thus a higher μ_{rec} value, than zircon. This grain has been identified as a Nb-Ta-U oxide mineral and indeed not as zircon. This Nb-Ta-U oxide, or previously described in Lehmann et al. (2008) as U-rich microlite, is one of the more rare Nb-Ta minerals present in the mineralized pegmatites, compared to the more common columbite-tantalite solid-solution series. However, this mineral could be locally concentrated in specific zones (Lehmann et al., 2008), and has been described to be characteristic for the Nb-Ta mineralization of the Gatumba area (Melcher et al., 2015).

Interrelationships and Orientation of Mineral Phases

Sample A presented in the previous section was further analyzed using a correlation matrix (Fig. 10) to investigate possible spatial correlations. For the 5 different segmented phases, 10 unique interrelationships could be calculated. The coefficient of variation (Fig. 11) was calculated for the 5 different segmented phases, which may give insights in the possible preferential orientation of minerals to deduce possible oriented growth or the so-called unidirectional solidification texture (UST) (Shannon et al., 1982). One of the main observations from Fig. 10 was the omnidirectional strong negative correlation between albite and quartz, which is to a lesser extent also observable between albite and muscovite. On the other hand, a positive (omnidirectional) correlation was observed between schorl/apatite and the dense mineral phase, which is here mostly zircon. In data plots of the correlation matrix where muscovite was considered (Fig. 10), the correlation was strongly influenced by the coefficient of variation of muscovite (Fig. 11). General low c_v values at an inclination of 90° were especially reflected in the correlation between muscovite and schorl/apatite and between muscovite and the dense mineral phase. The same was observed for c_v values of the dense mineral phase, where the deviating value at an azimuth of 90° and inclination of 45° is well reflected in the correlation matrix involving the dense mineral phase. A relative high c_v value at this orientation can be explained by the large Nb-Ta-U oxide grain (see Fig. 11) included within the group of otherwise much smaller dense

mineral grains. The influence of c_v was less pronounced for albite and quartz, since both phases only displayed low c_v values within a small range (respectively 0.154-0.45 and 0.127-0.372).

DISCUSSION

The combination of different imaging techniques, both 2D and 3D, has a strong application potential for the analysis of the mineralogy and geochemistry of rock samples down to the microscopic scale. Extending this into 3D allows for the study of mineral relationships and the quantification of morphological characteristics of minerals without stereological errors from 2D estimations. Recent existing practices in analyzing ore samples (e.g., Guntoro et al., 2019b; Warlo et al., 2021) demonstrate both the shortcomings as well as the benefits from combining SEM-EDX with µCT.

Polished sections were here analyzed with SEM-EDX to classify minerals with an AM system and the obtained mineral distribution maps were used to interpret their distribution in 3D. Sample preparation is especially necessary to perform SEM-based AM analyses, as this technique requires a well-polished surface coated with a sputtered carbon coating to produce high quality images (Reed, 2005). Besides, commercial SEM instrumentation often comes with standard sample holders, which limits the possible 3D volumes to be analyzed with both SEM and µCT. For our system, the diameter per sample is standard one inch and the sample is also limited in height to fit in the vacuum chamber. In addition, when scanning polished samples with µCT, image artifacts occur at the surface of samples due to the so-called cone-beam effect (Cnudde & Boone, 2013; Guntoro et al., 2019b). This effect will eventually alter the greyscale values and thus also limit the possible segmentation. To anticipate this, core samples with the same diameter, but extended in length, were scanned prior to any sample preparation. This allowed us to select a region of interest from the µCT data, in accordance with the polished sample, without having these image artifacts at the polished surfaces. By doing this, the information from an equivalent µCT slice of the polished surface can then be used to train the 3D Weka segmentation. Alternatively, optimized image acquisition (De Witte, 2010) and post-processing steps (Kazhdan et al., 2015) could be undertaken to remove some of these image artifacts at the surface of samples.

Despite the above-mentioned limitations of combining µCT with SEM-EDX, a SEM-EDX based AM system proved to be an important and needed part of the methodology to provide background information for the visual interpretation and/or segmentation of µCT data. SEM-based AM systems are commercially more and more well-established (Graham, 2017) and are increasingly applied in geological

studies (e.g., Warlo et al., 2019; Keulen et al., 2020). For minerals with a similar chemical composition, but with different crystalline structures (e.g., hematite and magnetite) or minerals which are not straightforward to classify using existing SEM-based AM systems (e.g., mineral polymorphs), one could consider XRD. XRD is a routinely performed, but destructive, laboratory technique that already has proven to be an essential tool for phase identification within geosciences (Artioli, 2018). Advanced developments in X-ray microscopy enabled the establishment of laboratory based diffraction contrast tomography (Holzner et al., 2016) which opens opportunities for further research in 3D materials science. An example where this could have been of benefit here, is the identification of the mineral that strongly resembled biotite in EDX spectrum (Fig. 7b), but which showed to have a density that was too low and, therefore, was classified as a Fe-Li mica. Although the Li-content of this mineral was not measurable with the used SEM equipment, as the elemental range of EDX is limited from beryllium to uranium, this chemical information could be inferred from the combination of SEM-based AM, µCT analyses and previous observations. Solely based on EDX spectra (Fig. 7b), this mineral could be interpreted as the iron end-member (annite) of the biotite mica group. However, the relative position of μ_{rec} in the µCT images shows that its value is too low to be classified as biotite. The calculated μ_{rec} is lower than these of apatite and schorl, which suggests the presence of a low atomic number element that significantly lowers its attenuation coefficient. Lithium is such an element that is known to be incorporated into mica minerals of corresponding pegmatites (Hulsbosch et al., 2013). Lepidolite and zinnwaldite, respectively containing 3.70-5.42 wt% and 2.19-3.72 wt% of Li_2O (John, n.d.), are the two most common Li-micas in cassiterite and topaz-bearing pegmatites (Dill, 2010) and were previously also observed in this mineralization (Hulsbosch et al., 2013). The relative position of μ_{rec} matches well with the simulated μ_{rec} value of zinnwaldite (Fig. 2b) and excludes lepidolite (μ_{rec} of lepidolite is too low). In this case, even powder XRD analysis would not give a decisive answer due to its resemblance with other mica minerals, especially when the co-existence of other micas is inevitable in the sample preparation. Only chemical data from e.g., laser ablation inductively coupled plasma mass spectrometry could give a decisive answer, but techniques like this are often not available or are too costly for routinely analyses.

By using XRD analysis, it would have been possible to narrow the possibilities down to a more specific mineral or mineral group. Although this may be of importance for the mineralogical interpretation of the data, this will hardly influence the segmentation of the µCT data. For the example of hematite (Fe_2O_3; ρ

390 = 5.23 g/cm³) and magnetite ($Fe^{2+}Fe_2O_4$; ρ = 5.20 g/cm³), μ_{rec} will be here almost the same (respectively
391 2.81 and 2.83).
392 The main advantage of mineral distribution maps acquired with TIMA-X is the possibility to directly
393 correlate this 2D mineralogical information with a 3D µCT dataset and to re-polish the sample to a
394 specific section of interest for verification. As an example, the mineral assemblage in Fig. 8 was checked
395 to see if the assumptions that were made from µCT images were correct. It is the interpretation of these
396 sought for 3D mineral assemblages that will help to further refine the paragenesis of ore deposits. On
397 top of that, similar to a mineral standards library that is built within AM systems, a list of identified
398 minerals can be deduced to build a library of linear attenuation coefficients μ_{lin} (see also Fig. 2a). Once
399 all possible minerals encountered for the ore deposit under consideration are known, a library of μ_{rec}
400 values can be calculated for a given µCT setup. It is just so that calculations of the linear attenuation
401 coefficient μ_{lin} are not sufficient to predict the behavior, or better the produced greyscale values, of the
402 different minerals in the µCT images. As visualized in Fig. 2a, this value depends largely on the energy
403 of radiation. Since the source of radiation is almost always polychromatic in lab-based systems (Cnudde
404 & Boone, 2013), combined with an energy-dependent detector sensitivity, a measure needs to be
405 calculated for a certain setup. A possibility is to calculate this based on the effective energy (Bam et al.,
406 2020), which is a weighted average of an actual polychromatic beam for a specific voltage and setup
407 (see Table 1). This was successfully applied in recent studies (Gibson et al., 2021; Warlo et al., 2021).
408 Although this assumption may be correct when considering the X-ray beam before entering the sample,
409 this X-ray beam is still a polychromatic beam that will be altered in terms of effective energy depending
410 on material composition and sample thickness. As also issued in Bam et al. 2020, this will affect the
411 expected discrimination between the minerals (see Fig. 12). To counter this issue, the effect of material
412 properties and sample thickness and the full polychromatic beam was here taken into account to
413 calculate μ_{rec} for each mineral (Fig. 2b). The μ_{rec} was calculated here on the assumption that a
414 monomineralic sample with a thickness of 2 cm (according to the used sample diameter in this study)
415 was scanned. Note that although these values proofed to serve as a perfect guidance for phase
416 segmentation, images are still prone to several systematic errors (e.g., noise, discretization effects,
417 imaging artifacts; Cnudde & Boone, 2013). Machine learning tools like Weka 3D segmentation
418 (Arganda-Carreras et al., 2017) are capable of dealing with some of these errors to improve the accuracy
419 of the segmented phases. By training a range of image features (e.g., edge detectors and texture filters)

it becomes possible to distinguish different phases from each other that may contain overlapping greyscale values (Fig. 13). Extending mineral phase segmentation to more advanced machine learning techniques (see e.g., Furat et al., 2019; Evsevleev et al., 2020) could provide even better results, but would require a more elaborate period of segmentation training.

The resulting segmented data can be quantified in 3D through a variation of data analysis methods (Guntoro et al., 2019a) to open up a new depth of information in describing textures of minerals. This allows for the 3D interpretation of both the individual phases and of the interrelationships between the different phases. In terms of ore geology, textural elements like size, shape, and orientation of mineral grains are referred to as structural textures, while the spatial relation between mineral phases is referred to as stationary texture (Lobos et al., 2016). The presented methodology covers both the quantitative extraction of structural textures (i.e., coefficient of variation as a measure of orientation; Fig. 11) and stationary textures (i.e., correlation matrix; Fig. 10) with a low computational expense. The employed script only required to open the segmented dataset 4 times at the same time: (± 7GB). Since this feature extraction does not take into account individual grains/minerals for its calculations, this could be immediately be applied to single/grouped greyscale values instead of more elaborately trained segmented datasets. The extraction of these features in such a manner opens possibilities to quantify datasets of whole core sections and/or of selected segments within these cores (e.g., vein orientation and correlation of mineral phases with ore minerals). As an example, one Nb-Ta-U oxide and multiple zircon grains were found to be associated with a stellate aggregate of muscovite that is strongly intergrown with a grouped occurrence of apatite (see Fig. 6b). It is this spatial association that caused the positive correlation between schorl/apatite and the dense mineral phase (Fig. 10).

CONCLUSIONS

In this work, we applied a comprehensive methodology for the characterization of the mineralogy of a Sn-Nb-Ta mineralization in 3D. First, a mineral library of all minerals present is derived from SEM-based AM analyses for the calculation of μ_{lin}. The deduced μ_{rec} serve as a most correct guidance to differentiate between different minerals for a given experimental µCT setup. For example, this allowed us to differentiate biotite from a Fe-Li mica due to the attribution of the low atomic element lithium. The trainable Weka 3D segmentation within the open-software Fiji environment allowed for data preparation and the differentiation between five separate phases (albite, quartz, muscovite, schorl/apatite & dense

mineral phase). Quantitative information on the orientation of individual mineral phases and their spatial correlation in 3D was provided by the calculation of statistical descriptors at a low computational expense. Combining μCT and an SEM-based AM system within a comprehensive methodology can aid in the mineralogical investigation of ore deposit, both in aspects of visualization and quantification at the microscopic scale.

Declarations

Compliance with Ethical Standards

Disclosure of potential conflicts of interest

Funding

This work is funded by the European Electron and X-ray Imaging Infrastructure (EXCITE), this project has received funding from the European Union's Horizon 2020 research and innovation programme under grant agreement No 101005611. SEM instrumentation has received funding from Research Foundation – Flanders (FWO) for medium-scale research infrastructure under grant agreement number I013118N.

Competing interests

The authors declare that they have no known competing financial interests or personal relationships that could have appeared to influence the work reported in this paper.

Research involving Human Participants and/or Animals

Not applicable

Informed consent

Not applicable

Data and code availability

The datasets and code generated during and/or analyzed during the current study are available from the corresponding author on reasonable request.

References

Ali, S. H., Giurco, D., Arndt, N., Nickless, E., Brown, G., Demetriades, A., Durrheim, R., Enriquez, M. A., Kinnaird, J., Littleboy, A., Meinert, L. D., Oberhänsli, R., Salem, J., Schodde, R., Schneider, G., Vidal, O. & Yakovleva, N. (2017). Mineral supply for sustainable development requires resource governance. *Nature*, 543, 367-372. https://doi.org/10.1038/nature21359

Arganda-Carreras, I. (2018). *Weka Segmentation tiling script*. Scientific Community Image Forum. https://forum.image.sc/t/trainable-wekaerror-large-images/10929.

Arganda-Carreras, I., Kaynig, V., Rueden, C., Eliceiri, K.W., Schindelin, J., Cardona, A. & Sebastian Sueng, H. (2017). Trainable Weka Segmentation: a machine learning tool for microscopy pixel classification. *Bioinformatics,* 33(15), 2424-2426. https://doi.org/10.1093/bioinformatics/btx180

Artioli, G. (2018). X-Ray Diffraction, Studies of Inorganic Compounds and Minerals. *Encyclopedia of Spectroscopy and Spectrometry,* 3, 676-683. http://doi.org/10.1016/B978-0-12-803224-4.00176-X

Bam, L.C., Miller, J.A. & Becker, M. (2020). A Mineral X-ray Linear Attenuation Coefficient Tool (MXLAC) to Assess Mineralogical Differentiation for X-ray Computed Tomography Scanning*. Minerals*, 10, 441. http://doi.org/10.3390/min10050441

Becker, M., Jardine, M.A., Miller, J.A. & Harris, M. (2016). X-ray Computed Tomography – a Geometallurgical Tool for 3D Textural Analysis of Drill Core?. In S. Dominy & L. O'Connor (eds.), *The Third AusIMM International Geometallurgy Conference 2016* (pp. 231-240). AusIMM.

Callow, B., Falcon-Suarez, I., Moreno-Marin, H., Bull, J.M. & Ahmed, S. (2020). Optimal X-ray micro-CT image based methods for porosity and permeability quantification in heterogeneous sandstones. *Geophysical Journal International*, 223(2), 1210-1229. https://doi.org/10.1093/gji/ggaa321

Chantler, C.T., Olsen, K., Dragoset, R.A., Chang, J., Kishore, A.R., Kotochigova, S.A., and Zucker, D.S. (2005), *X-Ray Form Factor, Attenuation and Scattering Tables* (version 2.1). [Online] National Institute of Standards and Technology, Gaithersburg, MD. https://doi.org/10.18434/T4HS32

Cnudde, V. & Boone, M.N. (2013). High-resolution X-ray computed tomography in geosciences: A review of the current technology and applications. *Earth-Science Reviews,* 123, 1-17. http://doi.org/10.1016/j.earscirev.2013.04.003

De Boever, W., Derluyn, H., Van Loo, D., Van Hoorebeke, L. & Cnudde, V. (2015). Data-fusion of high resolution X-ray CT, SEM and EDS for 3D and pseudo-3D chemical and structural characterization of sandstone. *Micron,* 74, 15-21. https://doi.org/10.1016/j.micron.2015.04.003

509 Dewaele, S., Henjes-Kunst, F., Melcher, F., Sitnikova, M., Burgess, R., Gerdes, A., Fernandez, M.A.,
510 De Clercq, F., Muchez, P. & Lehmann, B. (2011). Late Neoproterozoic overprinting of the cassiterite
511 and columbite-tantalite bearing pegmatites of the Gatumba area, Rwanda (Central Africa). *Journal of*
512 *African Earth Sciences,* 61(1), 10-26. https://doi.org/10.1016/j.jafrearsci.2011.04.004
513 De Witte, Y. (2010). *Improved and Practically Feasible Reconstruction Methods for High Resolution X-*
514 *ray Tomography*. (Doctoral dissertation, Ghent University, Ghent). Retrieved from http://lib.ugent.be/
515 catalog/rug01:001404410
516 Dill, H.G. (2010). The "chessboard" classification scheme of mineral deposits: Mineralogy and geology
517 from aluminum to zirconium. *Earth-Science Reviews,* 100, 1-420.
518 https://doi.org/10.1016/j.earscirev.2009.10.011
519 Dhaene, J., Pauwels, E., De Schryver, T., De Muynck, A., Dierick, M. & Van Hoorebeke, L. (2015). A
520 realistic projection simulator for laboratory based X-ray micro-CT. *Nuclear Instruments and Methods in*
521 *Physics Research B*, 342, 170-178. http://doi.org/10.1016/j.nimb.2014.09.033
522 Evsevleev, S., Paciornik, S. & Bruno, G. (2020). Advanced Deep Learning-Based 3D Microstructures
523 Characterization of Multiphase Metal Matrix Composites. *Advanced Engineering Materials*, 22,
524 1901197. https://doi.org/10.1002/adem.201901197
525 Furat, O., Wang, M., Neumann, M., Petrich, L., Weber, M., Krill III, C. E. & Schmidt, V. (2019). Machine
526 Learning Techniques for the Segmentation of Tomographic Image Data of Functional Materials.
527 *Frontiers in Materials*, 6, 145. https://doi.org/10.3389/fmats.2019.00145
528 Gessner, K., Blenkinsop, T., Sorjonen-Ward, P. (2018). Characterization of ore-forming systems –
529 advances and challenges. In Gessner, K., Blenkinsop, T. G. & Sorjonen-Ward, P. (eds), *Geological*
530 *Society, London, Special Publications*, 453, 1-6. https://doi.org/10.1144/SP453.16
531 Gibson, B., Nwaila G. & Petersen J. (2021). Characterization of a coarse synthetic silver ore as a model
532 ore material for heap leaching research. *Minerals Engineering,* 174, 107253.
533 https://doi.org/10.1016/j.mineng.2021.107253
534 Godel, B. (2013). High-Resolution X-Ray Computed Tomography and Its Application to Ore Deposits:
535 From Data Acquisition to Quantitative Three-Dimensional Measurements with Case Studies from Ni-
536 Cu-PGE Deposits. *Economic Geology,* 108(8), 2005-2019. https://doi.org/10.2113/econgeo.108.8.2005

Graham, S. D. (2017). Automated mineralogy – The past, present and future. In Kongoli F, Bradshaw, D., Waters, K., Starkey, J. & Silva, A.C. (eds.), *Sustainable Industrial Processing Summit SIPS 2017,* 4, 96-115.

Gu, L., Wang, N., Tang, X. & Changela, H. G. (2020). Application of FIB-SEM Techniques for the Advanced Characterization of Earth and Planetary Materials. *Scanning*, 2020, 8406917. https://doi.org/10.1155/2020/8406917

Guntoro, P.I., Ghorbani, Y., Koch, P.-H. & Rosenkranz, J. (2019a). X-ray Microcomputed Tomography (µCT) for Mineral Characterization: A Review of Data Analysis Methods. *Minerals*, 9(3), 32 p. https://doi.org/10.3390/min9030183

Guntoro, P.I., Tiu, G., Ghorbani, Y., Lund, C. & Rosenkranz, J. (2019b). Application of machine learning techniques in mineral phase segmentation for X-ray microcomputed tomography (µCT) data. *Minerals Engineering,* 142, 105882. https://doi.org/10.1016/j.mineng.2019.105882

Hayes, S. M. & McCullough, E. A. (2018). Critical minerals: A review of elemental trends in comprehensive criticality studies. *Resources Policy*, 59, 192-199. https://doi.org/10.1016/j.resourpol.2018.06.015

Holzner, C., Lavery, L., Bale, H., Merkle, A., McDonald, S., Withers, P., Zhang, Y., Juul Jensen, D., Kimura, M., Lyckegaard, A., Reischig, P. & Lauridsen, E.M. (2016). Diffraction Contrast Tomography in the Laboratory Applications and Future Directions. *Microscopy Today*, 24(4), 34-43. https://doi.org/10.1017/34 S1551929516000584

Hrstka, T., Gottlieb, P., Skála, R., Breiter, K. & Motl, D. (2018). Automated mineralogy and petrology – applications of TESCAN Integrated Mineral Analyzer (TIMA). *Journal of Geosciences,* 63, 47-63. https://doi.org/10.3190/jgeosci.250

Hulsbosch, N., Hertogen, J., Dewaele, S., Andre, L. & Muchez, P. (2013). Petrographic and mineralogical characterisation of fractionated pegmatites culminating in the Nb-Ta-Sn pegmatites of the Gatumba area (western Rwanda). *Geologica Belgica,* 16(1-2), 105-117.

Hulsbosch, N. & Muchez, P. (2020). Tracing fluid saturation during pegmatite differentiation by studying the fluid inclusion evolution and multiphase cassiterite mineralization of the Gatumba pegmatite dyke system (NW Rwanda). *Lithos,* 354-355, 105285. https://doi.org/10.1016/j.lithos.2019.105285

Jardine, M. A., Miller, J. A. & Becker, M. (2018). Coupled X-ray computed tomography and grey level co-occurrence matrices as a method for quantification of mineralogy and texture in 3D. *Computers and Geosciences,* 111, 105-117. https://doi.org/10.1016/j.cageo.2017.11.005

John W. Anthony, Richard A. Bideaux, Kenneth W. Bladh, and Monte C. Nichols (eds.), (n.d.). *Handbook of Mineralogy* [online]. Mineralogical Society of America, Chantilly, VA, USA. http://www.handbookofmineralogy.org/.

Kazhdan, M., Lillaney, K., Roncal, W., Bock, D., Vogelstein, J. & Burns, R. (2015). Gradient-Domain Fusion for Color Correction in Large EM Image Stacks. *ArXiv*, 1506.02079. https://doi.org/10.48550/arXiv.1506.02079

Ketcham, R. A. & Mote, A. S. (2019). Accurate Measurement of Small features in X-ray CT Data Volumes, Demonstrated Using Gold Grains. *Journal of Geophysical Research: Solid Earth,* 124, 3508-3529. https://doi.org/10.1029/2018JB017083

Keulen, N., Malkki, S.N. & Graham, S. (2020). Automated Quantitative Mineralogy Applied to Metamorphic Rocks. *Minerals,* 10, 47. https://doi.org/10.3390/min10010047

Kyle, J.R. & Ketcham, R.A. (2015). Application of high resolution X-ray computed tomography to mineral deposit origin, evaluation, and processing. *Ore Geology Reviews,* 65(4), 821-839. http://doi.org/10.1016/j.oregeorev.2014.09.034

Laforce, B., Vermeulen, B., Garrevoet, J., Vekemans, B., Van Hoorebeke, L., Janssen, C. & Vincze, L. (2016). Laboratory Scale X-ray Fluorescence Tomography: Instrument Characterization and Application in Earth and Environmental Science. *Analytical Chemistry,* 88(6), 3386-3391. https://doi.org/10.1021/acs.analchem.6b00137

Lehmann, B., Halder, S., Ruzindana Munana, J., Ngizimana, J. & Biryabarema, M. (2014). The geochemical signature of rare-metal pegmatites in Central Africa: Magmatic rocks in the Gatumba tin-tantalum mining district, Rwanda. *Journal of Geochemical Exploration,* 144, 528-538. http://doi.org/10.1016/j.gexplo.2013.11.012

Lehmann, B., Melcher, F., Sitnikova, M. A. & Ruzindana Munana J. (2008). The Gatumba rare-metal pegmatites: chemical signature and environmental impact. *Études Rwandaises,* 16, 25-40.

Lobos, R., Silva, J. F., Ortiz, J. M., Díaz, G. & Egaña, A. (2016). Analysis and Classification of Natural Rock Textures based on New Transform-based Features. *Mathematical Geosciences,* 48(7), 835-870. https://doi.org/10.1007/s11004-016-9648-8

595 Masschaele, B., Dierick, M., Van Loo, D., Boone, M.N., Brabant, L., Pauwels, E., Cnudde, V. & Van
596 Hoorebeke, L. (2013). HECTOR: A 240kV micro-CT setup optimized for research. *Journal of Physics:*
597 *Conference Series,* 463, 012012. https://doi.org/10.1088/1742-6596/463/1/012012
598 Melcher, F., Graupner, T., Gäbler, H.-E., Sitnikova, M., Henjes-Kunst, F., Oberthür, Gerdes, A. &
599 Dewaele, S. (2015). Tantalum-(niobium-tin) mineralisation in African pegmatites and rare metal granites:
600 Constraints from Ta-Nb oxide mineralogy, geochemistry and U-Pb geochronology. *Ore Geology*
601 *Reviews,* 64, 667-719. http://doi.org/10.1016/j.oregeorev.2013.09.003
602 Otsu, N. (1979). A Threshold Selection Method from Gray-Level Histograms. *IEEE Transactions on*
603 *Systems, Man and Cybernetics,* 9(1), 62-66.
604 Pearce, M.A., Godel, B.M., Fisher, L.A., Schoneveld, L.E., Cleverley, J.S., Oliver, N.H.S. & Nugus, M.
605 (2018). Microscale data to macroscale processes: a review of microcharacterization applied to mineral
606 systems. In Gessner, K., Blenkinsop, T. G. & Sorjonen-Ward, P. (eds), *Geological Society, London,*
607 *Special Publications*, 453(1), 7-39. https://doi.org/10.1144/SP453.3
608 Reed, S. J. B. (2005). *Electron Microprobe Analysis and Scanning Electron Microscopy in Geology* (2nd
609 ed.) Cambridge University Press.
610 Reuter, M.A., van Schaik, A., Gutzmer, J., Bartie, N. & Abadías-Llamas, A. (2019). Challenges of the
611 Circular Economy: A Material, Metallurgical, and Product Design Perspective. *Annual Review of*
612 *Materials Research,* 49, 253-274. https://doi.org/10.1146/annurev-matsci-070218-010057
613 Reyes, F., Lin, Q., Udoudo, O., Dodds, C., Lee, P.D. & Neethling, S. (2017). Calibrated X-ray
614 microtomography for mineral ore quantification. *Minerals Engineering,* 110, 122-130.
615 https://doi.org/10.1016/j.mineng.2017.04.015
616 Schindelin, J., Arganda Carreras, I., Frise, E., Kaynig, V., Longair, M., Pietzsch, T., Preibisch, S.,
617 Rueden, C., Saalfeld, S., Schmid, B., Tinevez, J.-Y., White, D.J., Hartenstein, V., Eliceiri, K., Tomancak,
618 P. & Cardona, A. (2012). Fiji: an open-source platform for biological-image analysis. *Nature Methods,*
619 9, 676-682. https://doi.org/10.1038/nmeth.2019
620 Shannon, J.R., Walker, B.M., Carten, R.B. & Geraghty, E.P., 1982. Unidirectional solidification textures
621 and their significance in determining relative ages of intrusions at the Henderson Mine, Colorado.
622 *Geology*, 10(6), 293-297. https://doi.org/10.1130/0091-7613(1982)10<293:USTATS>2.0.CO;2

Strzelecki, P.J., Świerczewska, A., Kopczewska, K., Fheed, A., Tarasiuk, J. & Wroński, S. (2021). Decoding Rocks: An Assessment of Geomaterial Microstructure Using X-ray Microtomography, Image Analysis and Multivariate Statistics. *Materials,* 14, 3266. https://doi.org/10.3390/ma14123266

Vlassenbroeck, J., Dierick, M., Masschaele, B., Cnudde, V., Van Hoorebeke, L. & Jacobs, P. (2007). Software tools for quantification of X-ray microtomography at the UGCT. *Nuclear Instruments and Methods in Physics Research A*, 580(1), 442-445. https://doi.org/10.1016/j.nima.2007.05.073

Wang, Y. & Miller, J.D. (2020). Current developments and applications of micro-CT for the 3D analysis of multiphase mineral systems in geometallurgy. *Earth-Science Reviews,* 211, 103406. https://doi.org/10.1016/j.earscirev.2020.103406

Warlo, M., Wanhainen, C., Bark, G., Butcher, A.R., McElroy, I., Brising, D. & Rollinson, G. K. (2019). Automated Quantitative Mineralogy Optimized for Simultaneous Detection of (Precious/Critical) Rare Metals and Base Metals in A Production-Focused Environment. *Minerals,* 9, 440. https://doi.org/10.3390/min9070440

Warlo, M., Bark, G., Wanhainen, C., Butcher, A.R., Forsberg, F., Lycksam, H., & Kuva, J. (2021). Multi-scale X-ray computed tomography analysis to aid automated mineralogy in ore geology research. *Frontiers in Earth Science,* 9, 789372. https://doi.org/10.3389/feart.2021.789372

Wellmer, F-W., Buchholz, P., Gutzmer, J., Hagelüken, C., Herzig, P., Littke, R. & Thauer, R. K. (2019). *Raw Materials for Future Energy Supply*. Springer Cham. https://doi.org/10.1007/978-3-319-91229-5

Table captions

Table 1 Experimental setup of the µCT scans.

Figure captions

Fig. 1 Overview of the different steps that were undertaken for the segmentation of the different mineral phases.

Fig. 2 Calculated attenuation coefficients of all minerals possibly present. (a) Linear attenuation coefficients (μ_{lin}) of the studied mineral assemblages as a function of X-ray energy. (b) Reconstructed attenuation coefficients (μ_{rec}) as calculated for the given experimental setup and sample size. The FFAST database maintained by the National Institute of Standards and Technology (NIST) (Chantler et al., 2005), and available online at physics.nist.gov/PhysRefData/FFast/html/form.html, allows to calculate μ_{lin} as a function of energy. Density values for the different mineral phases are derived from

653 the calculated densities in the handbook of mineralogy (John, n.d.) and is available online at
654 handbookofmineralogy.org.

655 **Fig. 3** Procedure of post-processing the segmented µCT data. (a) Original µCT slice where lighter gray
656 values correspond with higher μ_{rec} values. (b) Data preparation by automatic thresholding and binary
657 morphological operations. (c) Mineral phase segmentation using Weka 3D segmentation. (d)
658 Segmented dataset after post-processing. (e-g) Detailed excerpt (see Fig. 3c) of how intermediate
659 mineral phases are removed from the segmented dataset. (f) Removed datapoints of where an
660 intermediate phase coincides with the area overlapped by both the low density phase and high density
661 phase after a single dilation (morphological operation). (g) Final segmented image where misclassified
662 intermediate phases (see e.g., removed rim of intermediate phase around high density phase) are
663 excluded for further feature extraction.

664 **Fig. 4** Virtual sample (X:Y:Z = 9×9×9) containing a segmented phase A (9×2×2). The coefficient of
665 variation is 0 for phase A when measured along the X-axis (as the values of A remain constant, i.e., Y:Z
666 = 2×2), while the coefficient of variation is 1.87 for phase A when measured along the Y- or Z-axis (i.e.,
667 the measured values are here either 0 or 9×2).

668 **Fig. 5** Outline for the visualization of oriented statistical measures. (a) Orientation of resliced data by
669 using two angular measurements. (b) Data plot of 3D statistical measures (in the image of stereonets
670 for the representation of 3D structural geological analysis).

671 **Fig. 6** Mineral distribution map of sample A (acquired with TIMA-X) with the corresponding µCT slice.
672 (a) BSE image. (b) Mineral distribution map. (c) Calculated μ_{rec} values for the identified (color coded)
673 minerals in the mineral distribution map. (d) Corresponding µCT slice.

674 **Fig. 7** Comparison of the measured and simulated EDX spectra of (a) muscovite and (b) minerals that
675 classify as Fe-Li mica (zinnwaldite) following the AM system.

676 **Fig. 8** (a) A µCT slice of sample B with some of the most important identified mineral phases indicated.
677 Note that the greyscale values are adjusted to the range of values present within this slice (see Fig. 6c
678 for relative position of μ_{rec} for each indicated mineral). (b) 3D visualization of the elongated assemblage
679 of albite, quartz, muscovite, and schorl in Fig.8a and where the different phases are indicated according
680 to their colors used in Fig. 6 (grid size = 5 mm).

681 **Fig. 9** Volume rendering of the different segmented phases within sample A (grid size = 5 mm).

682 **Fig. 10** Correlation matrix of the different segmented phases within sample A (see Fig. 9).

683 **Fig. 11** Coefficient of variation for each segmented phase of sample A (see Fig. 9). Note that each
684 segmented mineral phase displays a different range of values.

685 **Fig. 12** Extreme example of the influence of material composition and sample thickness on the relative
686 position of μ_{rec} for three minerals that were encountered during SEM-EDX analyses.

687 **Fig. 13** Distribution of greyscale values for each segmented phase in sample A. The eroded data points
688 coincide with local maxima at the intersection between two segmented phases.

689

690 Table 1

Voltage	120 kV
Power	10 W
Projections	2400
Filter	Al 1 mm
Exposure time	1000 ms
Spatial resolution	18 µm

691

692 Figure 1

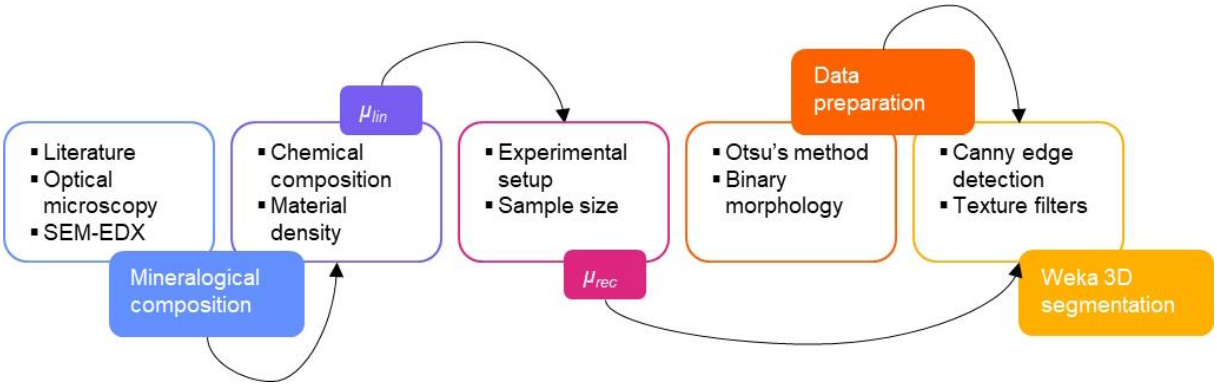

693

694

695 Figure 2

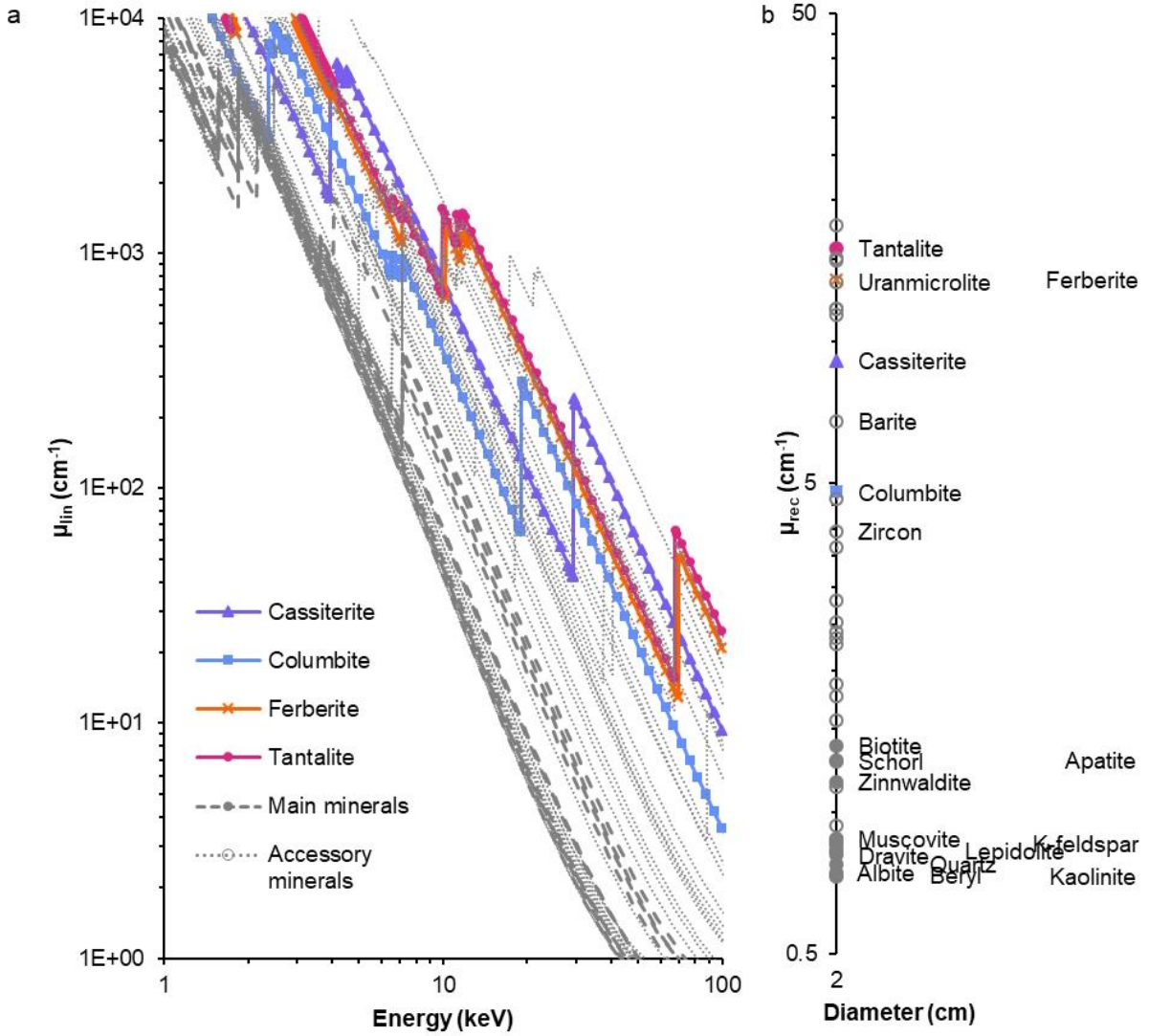

696

697

698 Figure 3

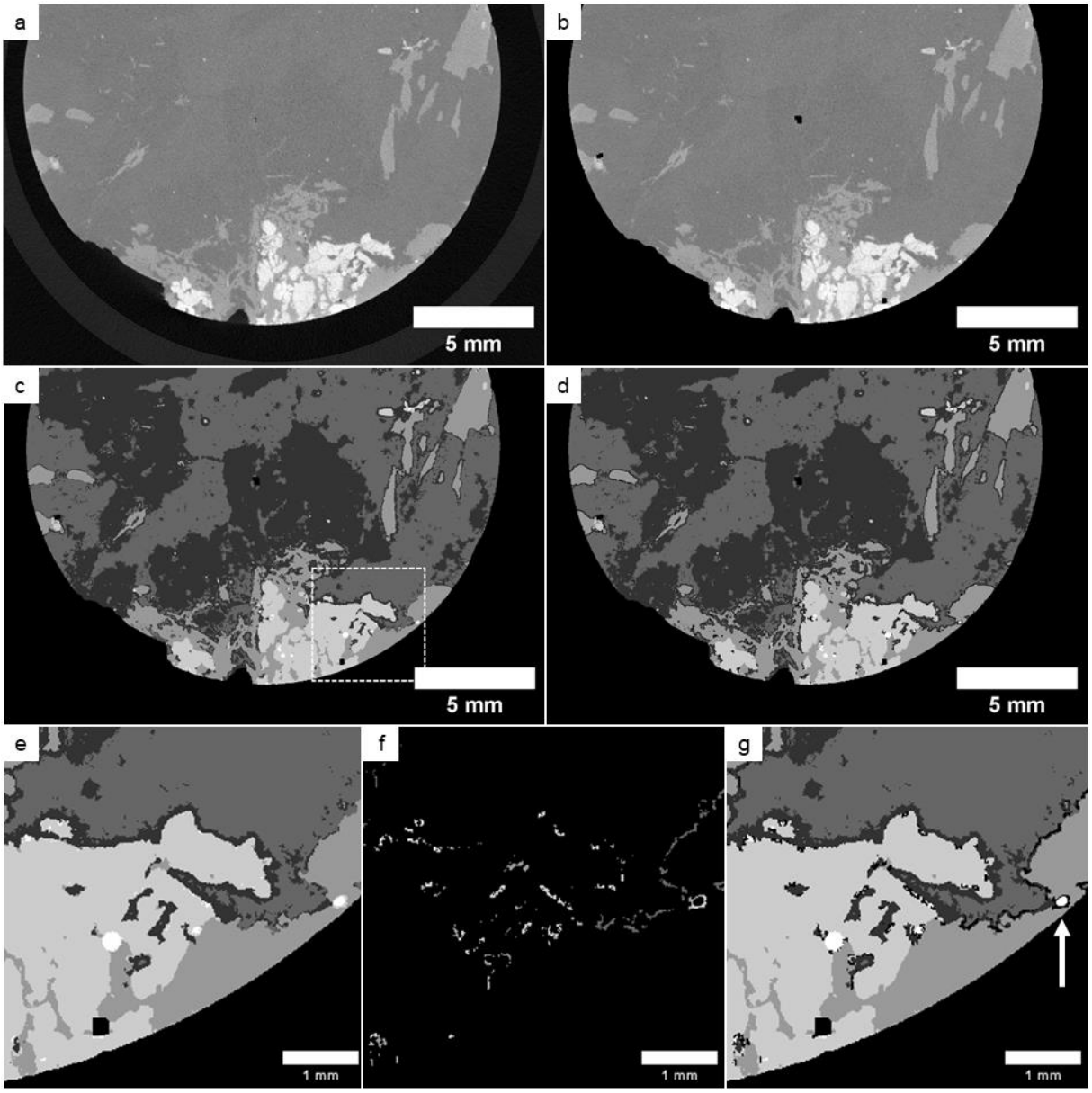

699

700

701 Figure 4

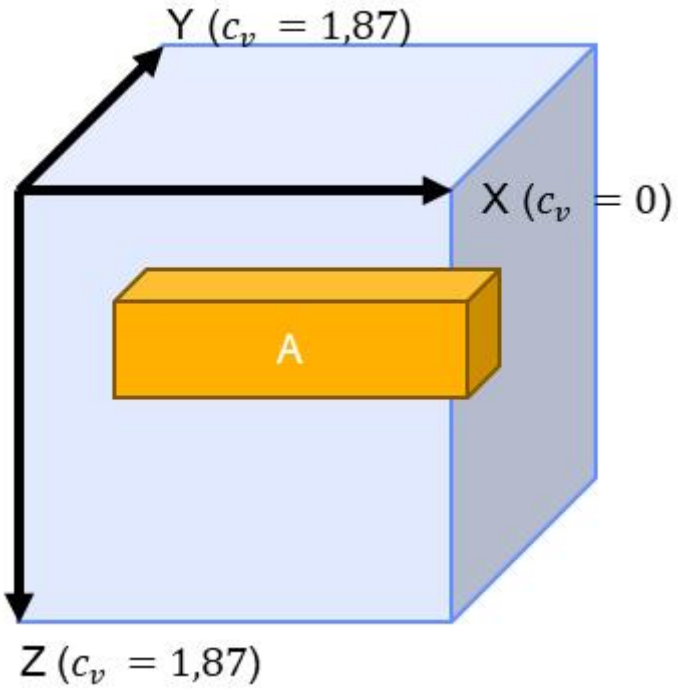

702

703

704 Figure 5

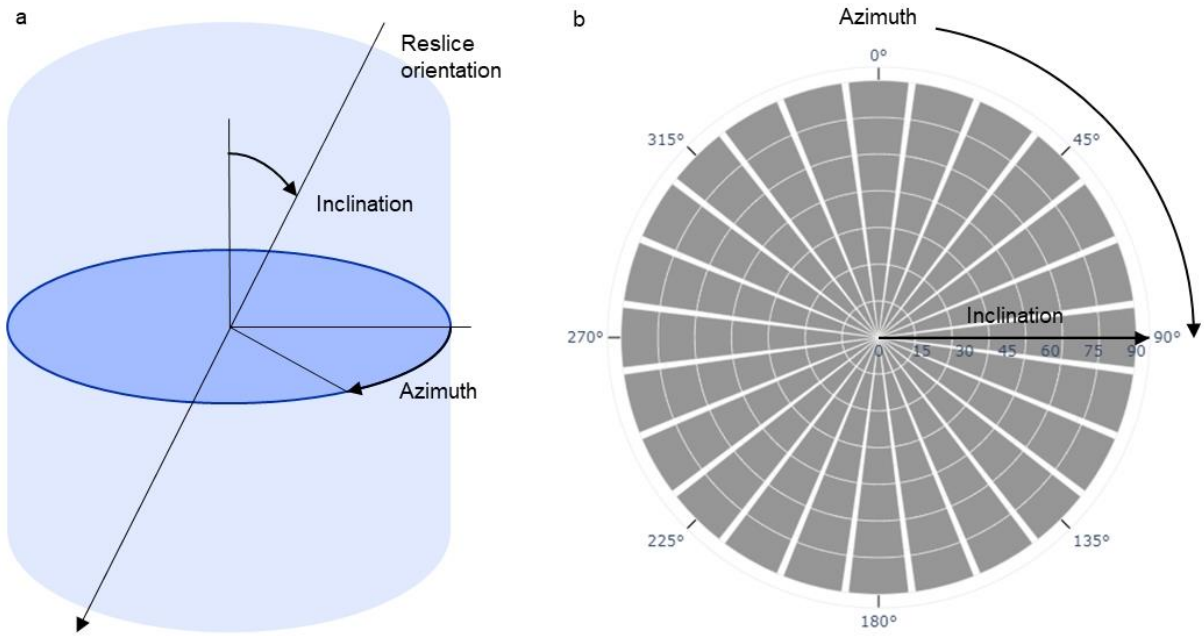

705

706

707 Figure 6

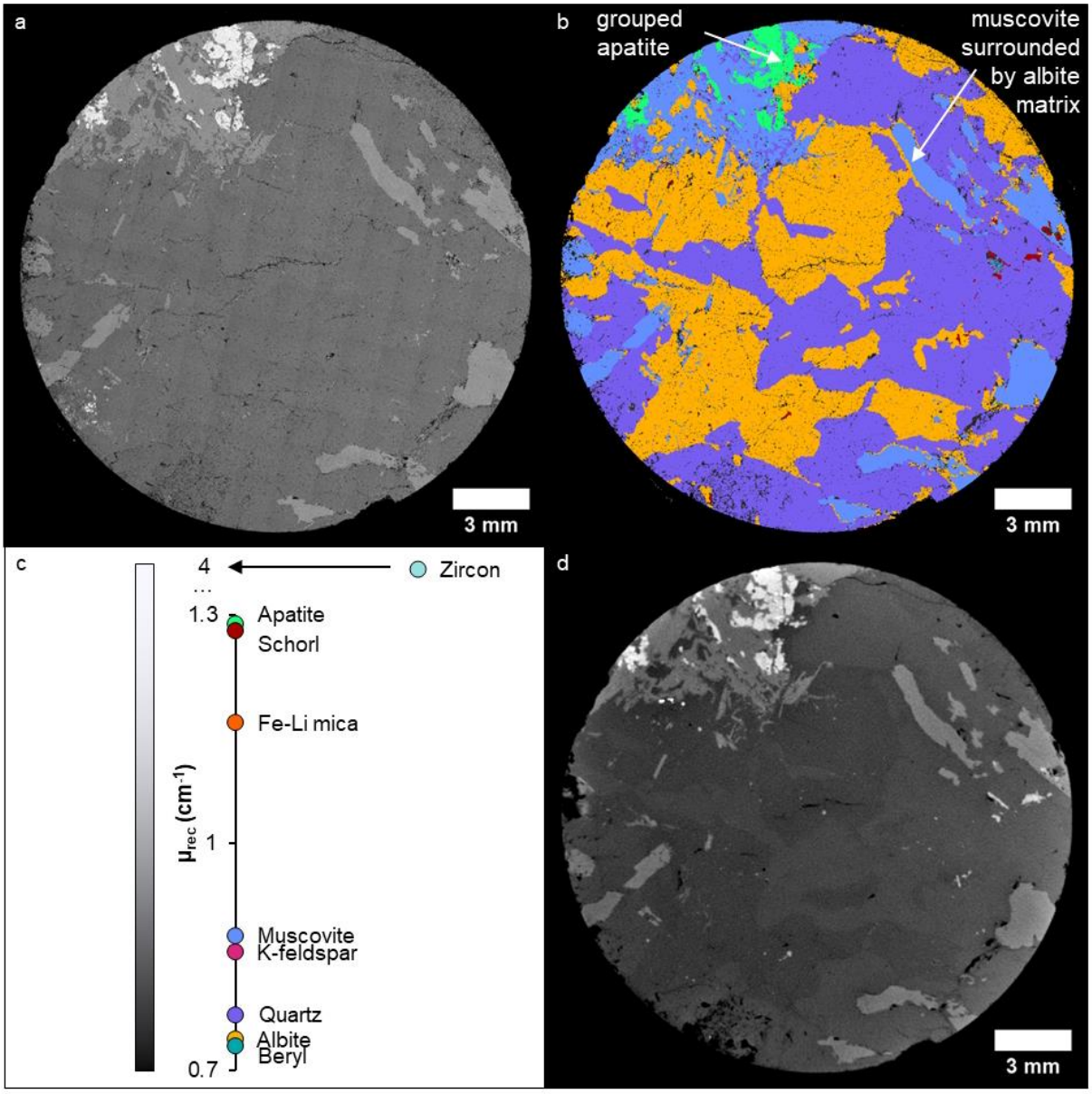

708

709

710 Figure 7

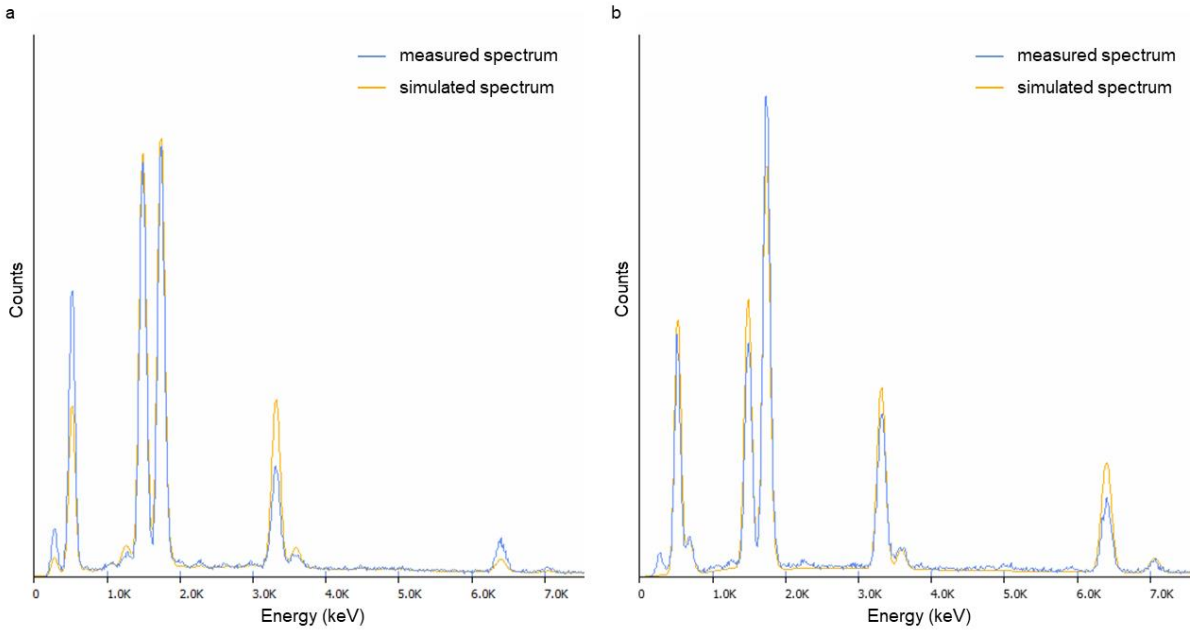

711

712

713 Figure 8

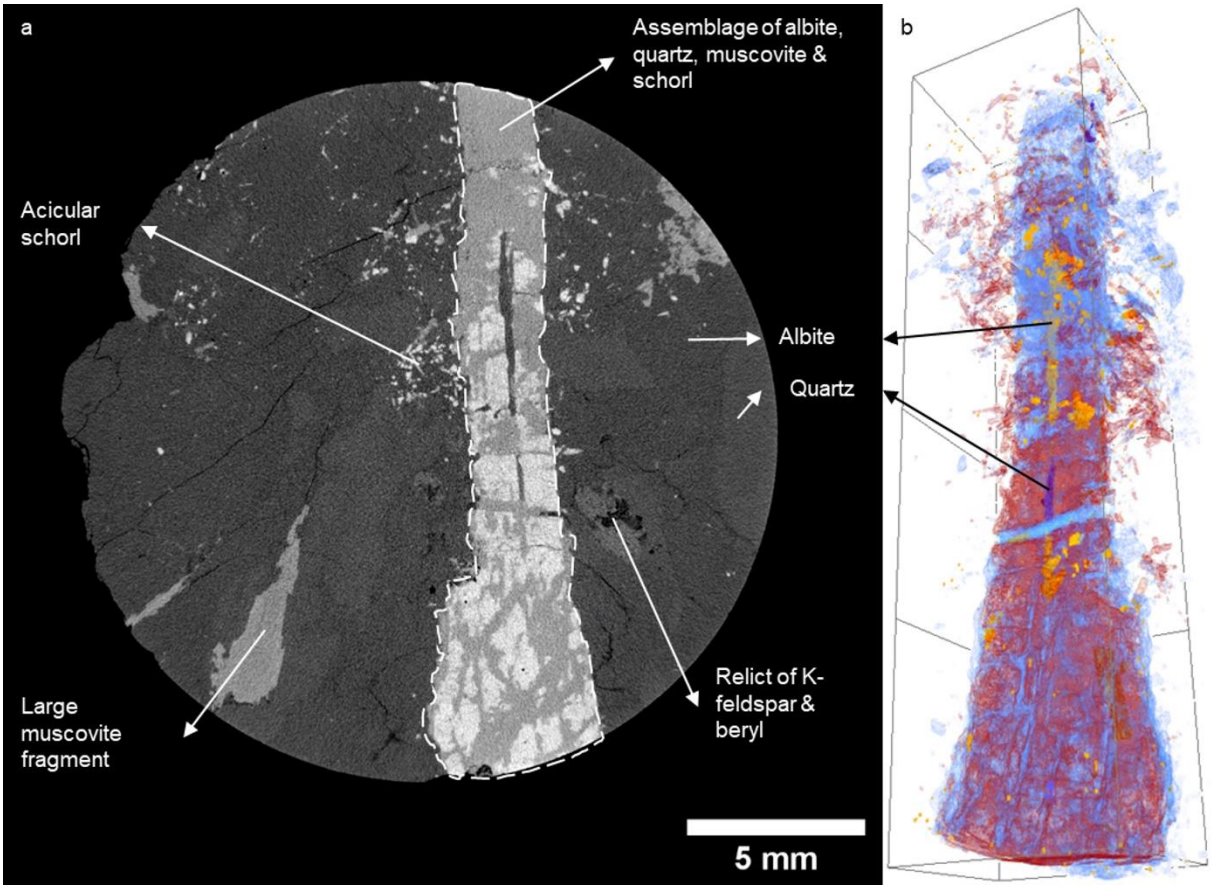

714

715

716 Figure 9

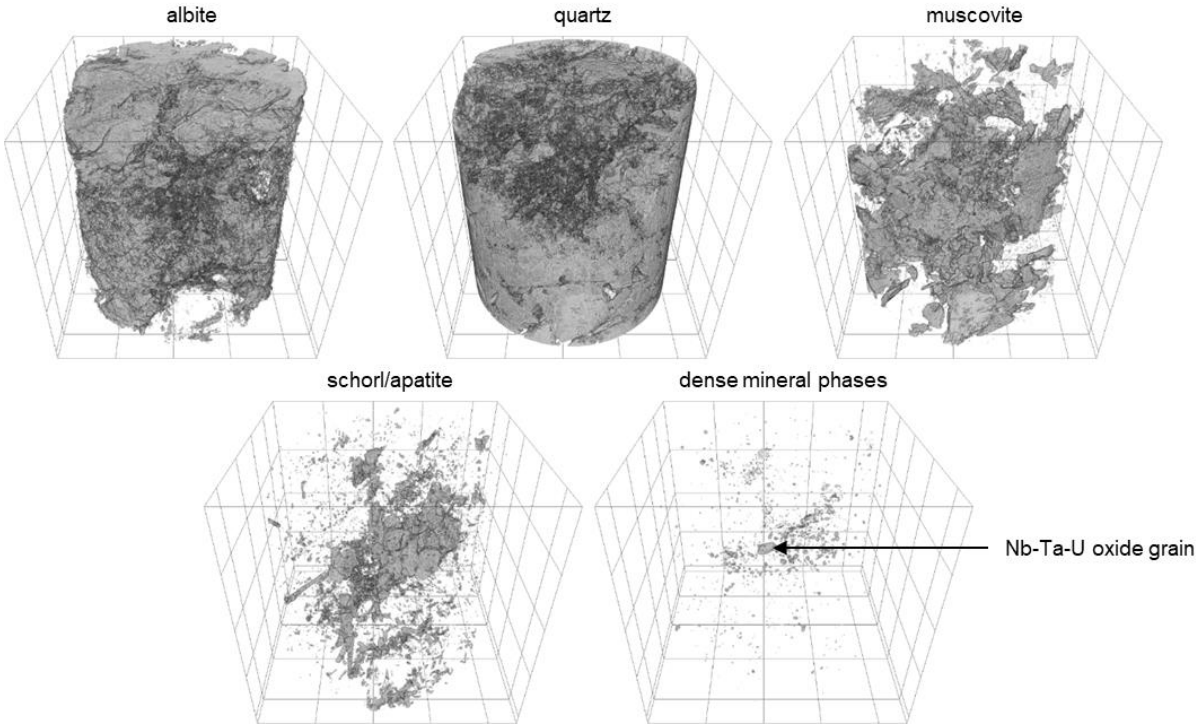

717

718

719 Figure 10

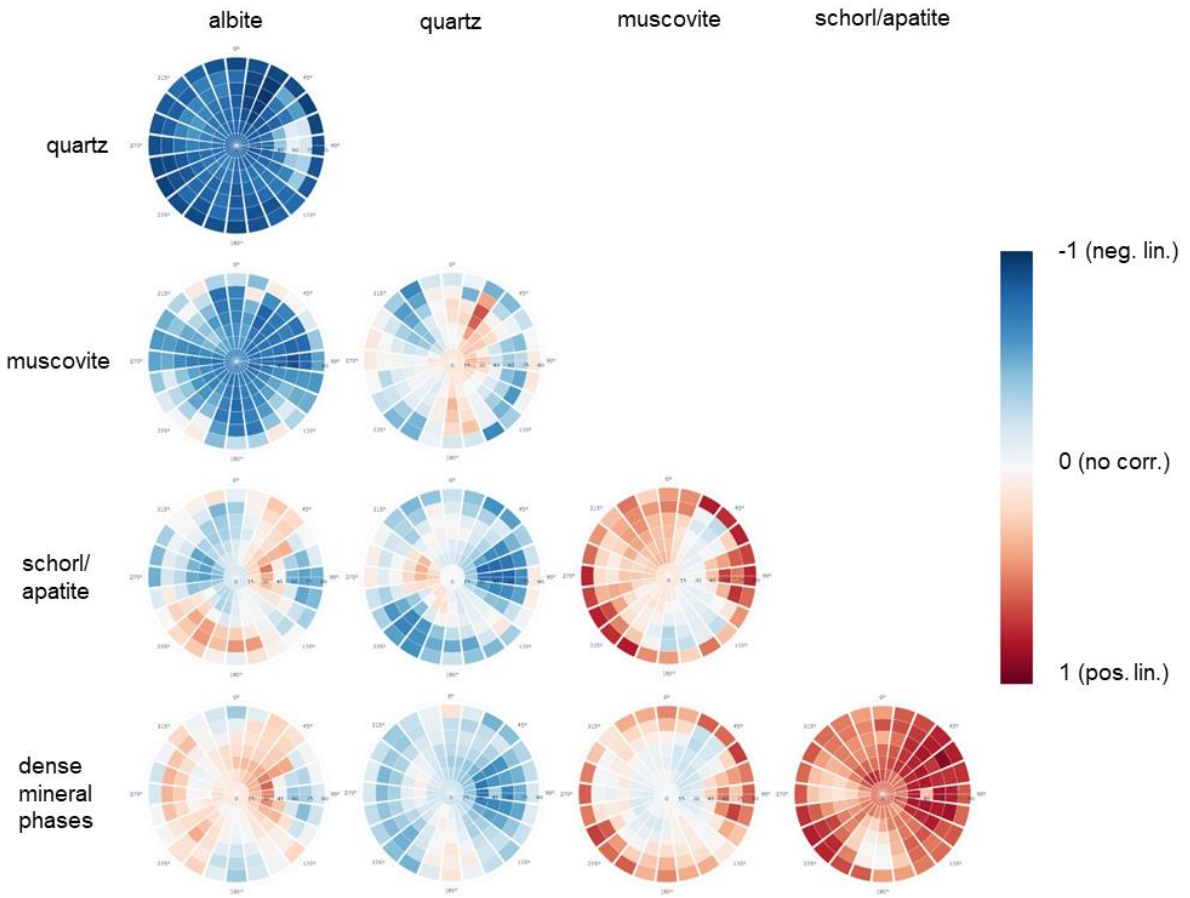

720

721

722 Figure 11

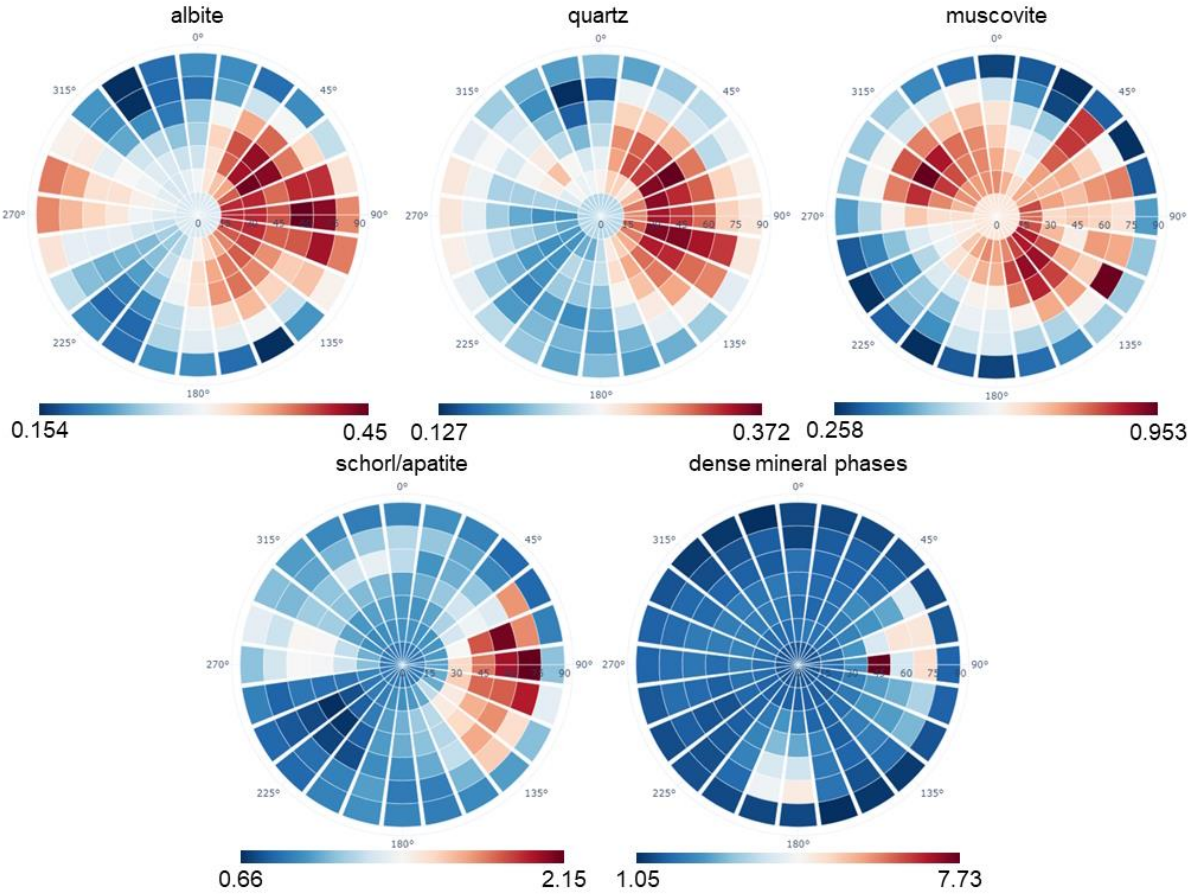

723